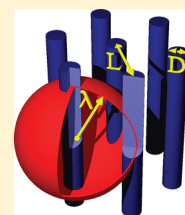


# Continuum Theory for Cluster Morphologies of Soft Colloids

A. Košmrlj,<sup>†,‡</sup> G. J. Pauschenwein,<sup>\*,†,§</sup> G. Kahl,<sup>||</sup> and P. Ziherl<sup>⊥,‡</sup><sup>†</sup>Massachusetts Institute of Technology, Cambridge, Massachusetts 02139-4307, United States<sup>§</sup>Austrian Institute of Technology, Energy Department, Giefinggasse 2, A-1210 Wien, Austria<sup>||</sup>Institut für Theoretische Physik and Center for Computational Materials Science, Technische Universität Wien, Wiedner Hauptstrasse 8-10, A-1040 Wien, Austria<sup>⊥</sup>Faculty of Mathematics and Physics, University of Ljubljana, Jadranska 19, SI-1000 Ljubljana, Slovenia<sup>#</sup>Jožef Stefan Institute, Jamova 39, SI-1000 Ljubljana, Slovenia

**ABSTRACT:** We introduce a continuum description of the thermodynamics of colloids with a core-corona architecture. In the case of thick coronas, their overlap can be treated approximately by replacing the exact one-particle density distribution by a suitably shaped step profile, which provides a convenient way of modeling the spherical, columnar, lamellar, and inverted cluster morphologies predicted by numerical simulations and the more involved theories. We use the model to study monodisperse particles with the hard-core/square-shoulder pair interaction as the simplest representatives of the core-corona class. We derive approximate analytical expressions for the enthalpies of the cluster morphologies which offer a clear insight into the mechanisms at work, and we calculate the lattice spacing and the cluster size for all morphologies of the phase sequence as well as the phase-transition pressures. By comparing the results with the exact crystalline minimum-enthalpy configurations, we show that the accuracy of the theory increases with shoulder width. We discuss possible extensions of the theory that could account for the finite-temperature effects.



## INTRODUCTION

A classical statistical-mechanical ensemble of particles with pairwise hard-core/square-shoulder interparticle potential

$$U(r) = \begin{cases} \infty, & r < \sigma \\ \varepsilon, & \sigma < r < \lambda \\ 0, & r > \lambda \end{cases} \quad (1)$$

(where  $\sigma$  and  $\lambda > \sigma$  are the core and the shoulder width, respectively, and  $\varepsilon > 0$  is the shoulder height) was introduced more than three decades ago as a model for the nonmonotonic melting line observed in elemental cesium and cerium.<sup>1,2</sup> The step-shaped repulsion is a stripped-down variant of a similar pair potential first discussed in connection with fluids with several phase transitions as well as the isostructural solid-solid phase transitions.<sup>3–6</sup> It is one of the simplest core-softened interparticle interactions, many of which were studied in great detail.<sup>7</sup> Recently, the relevance of the hard-core/square-shoulder potential has been explored primarily within the context of novel colloidal and nanocolloidal systems. At large enough densities, soft nanoscopic particles such as star polymers, self-assembled dendrimer micelles, and diblock copolymer micelles form various non-close-packed lattices<sup>8–13</sup> and quasicrystals.<sup>11,14</sup> The stability of these structures cannot be explained in terms of the Derjaguin-Landau-Verwey-Overbeek theory based on the van der Waals attraction and screened electrostatic repulsion<sup>15</sup> which cannot account for the interpenetration of the polymer-brush coronas that constitute the outer shell of nanocolloids. A more elaborate effective pair potential is needed, and in the theories associating the structure of condensed phases with the shape of the

interparticle repulsion, the hard-core/square-shoulder model plays an important role. With a single energy scale and two length scales, it is most likely the simplest refinement of the hard core and the inverse power repulsion that can generate some of the structural complexity seen in soft colloids.

Despite the seemingly plain pair potential, the hard-core/square-shoulder system is far from completely understood. The miscellany of methods which contributed to a better insight into its behavior include thermodynamic perturbation theory for both the liquid phase and the solid phases,<sup>16</sup> numerical simulations,<sup>17–19</sup> and analysis of minimal-energy  $T = 0$  configurations (MECs).<sup>20</sup> The common message of the early studies, which mostly focused on the narrow shoulder regime (typically,  $\lambda$  did not exceed  $1.5\sigma$ ),<sup>1,2</sup> is that the precise phase sequence is very sensitive to the exact width of the shoulder.<sup>20</sup> Only later did it become clear that for broad shoulders the model becomes considerably more robust: The low-density and the high-density close-packed structures were shown to be separated by a universal sequence of cluster phases<sup>17,18,21</sup> often referred to as *mesophases*.

Among the available theoretical methods to investigate this phase behavior, the search for MECs has always held a special place. In part, the reason for this is that MECs provide an efficient preliminary scan of the possible structures expected in the solid part of the phase diagram at finite temperatures. However, as the shoulder range is broadened, finding MECs becomes

**Special Issue:** Clusters in Complex Fluids

**Received:** September 15, 2010

**Revised:** January 5, 2011

**Published:** March 08, 2011

increasingly more difficult because each particle typically interacts with a large number of neighbors far beyond the first shell. Even with the most automatized and unbiased approaches such as genetic algorithms,<sup>22,23</sup> a systematic classification of MECs is complicated because they include a large number of crystal lattices of various degrees of complexity. Many of them are decorated by elaborate bases<sup>22–25</sup> which all share a distinct feature: The sites are located in a small part of the unit cell rather than distributed across all of it (Figure 1), and the bases of neighboring cells may be contiguous (Figure 1b,c), thereby forming lamellae and columns. Little imagination is needed to recognize the spherical, columnar, and lamellar clusters in the exact MECs,<sup>22–25</sup> and the features of the three morphological classes are far more striking than the exact lattice symmetry of MECs in question. Irrespective of the range of soft repulsion, the spherical, columnar, lamellar, and inverted morphologies intervene between the open FCC lattice at low pressures and the compact lattices at high pressures which terminate with a close-packed structure.<sup>24,25</sup>

At finite temperatures, the nonzero entropy of the hard-core/square-shoulder ensemble will gradually wash out many of the fine structural details of MECs but it is reasonable to expect that their large morphological features—especially the spherical, columnar, lamellar, etc., shape of clusters—will remain unaltered. For example, thermal jiggling of particles within the sphere-like clusters shown in Figure 1a will smooth their discrete  $T = 0$  spatial distribution across the volume of the cluster. As the temperature is increased, the probability of finding a particle at a point within the spherical envelope of a cluster will become more and more uniform, whereas the integrity of clusters themselves will not be affected. Similarly, the finite-temperature variant of the delicate spiral motif chosen to illustrate the complexity of MECs (Figure 1c) will be characterized by an increasingly more uniform particle distribution within the cylindrical surface enclosing the spiral, thereby emphasizing its columnar nature.

These considerations suggest that a coarse-grained, continuum model of the minimum-energy mesophase configurations could offer a better insight: By capturing their main morphological features, it may provide a description of the system more viable than the exact MECs themselves, as it will not expose the details of the intracluster structure most likely not very prominent at finite temperatures. Indeed, a comparison of the exact 2D MECs<sup>22,23</sup> and the snapshots of the finite-temperature structures in the broad-shoulder regime<sup>21</sup> offers a very convincing rationale for such a model. In both cases, the density is finite only within the well-defined regions of space and, if we choose to focus on the coarse-grained model, the one-particle density profile can be approximated by a step function of suitable carrier shape. The characteristic length scale is bound to be given by the shoulder width, simply because there is no other intrinsic distance in the model.

In this paper, we introduce the main ideas of the continuum description of the mesophases formed by the hard-core/square-shoulder ensemble and present both the 2D and 3D variants of the model. We also discuss the possibilities of extending it to finite temperatures and its application to pair interactions similar to the square-shoulder potential (eq 1). Throughout the paper, we emphasize that the continuum model can often be cast into an approximate analytical form, thereby providing a rather clear insight into the thermodynamics of the mesophases. In this respect, this approach is superior to direct numerical simulations and exact minimization methods.

## THE MODEL

The main idea of the continuum theory of hard-core/soft-shoulder particles, applicable to pair potentials with a broad shoulder, is simple and intuitive. If the ensemble undergoes a microphase separation whereby particles cluster in well-defined regions of space, each particle within a cluster overlaps with many neighbors, which may belong either to the same or a nearby cluster. Thus, the mean total potential experienced by the particles is a well-defined quantity insensitive to their precise arrangement within the clusters. If so, we can replace the exact discrete distribution of particles by a continuous density profile  $\theta(\mathbf{r})$  so that

$$N = \rho_{\text{eff}} \int_V \theta(\mathbf{r}) \, dV \quad (2)$$

where  $N$  is the number of particles in the volume of interest  $V$ ,  $\theta(\mathbf{r})$  is a step function such that  $\theta(\mathbf{r}) = 1$  within the clusters and  $\theta(\mathbf{r}) = 0$  elsewhere, and  $\rho_{\text{eff}}$ , the effective density, is the density of particles within the clusters. Given that the clusters do not occupy the whole volume, the effective density must be larger than the average number density  $\rho = N/V$ .

On the basis of the above assumptions, we evaluate the enthalpies of the spherical, cylindrical, lamellar, and inverted morphologies. We (i) parametrize each morphology by characteristic cluster size (i.e., sphere and cylinder diameter, lamellae thickness, or void diameter) and lattice spacing, (ii) compute the intracluster and the intercluster overlap energies and the corresponding enthalpies of all the morphologies, and use them to (iii) construct the  $T = 0$  phase diagram which also includes the uniform phase stable at high pressures. Both the intracluster and intercluster terms depend on the shape and volume of the overlap zone defined as the cross section of the cluster and the sphere representing the shoulder repulsion of the particle in question. The overlap zone depends on the position of the particle within the cluster as well as on the cluster shape itself, and the final overlap energy is obtained by averaging over all positions of the particle. The evaluation of the intra- and intercluster overlap energy is a matter of elementary geometry and thus rather straightforward although in some cases tedious.

All these calculations are subject to the constraint imposed by the hard-core part of the pair potential (eq 1) which demands that the effective number density within the clusters does not exceed the close-packing density

$$\rho_{\text{max}}^{2\text{D}} = \frac{2}{\sqrt{3}\sigma^2} \quad (3)$$

in 2D and

$$\rho_{\text{max}}^{3\text{D}} = \frac{\sqrt{2}}{\sigma^3} \quad (4)$$

in 3D. Within our theory, this is the only effect of the hard-core interactions on the mesophase morphologies. In all calculations, we also assume that the characteristic size of the clusters is smaller than the shoulder width, which somewhat simplifies the analysis. We show *a posteriori* that this is indeed the case.

The replacement of the discrete distribution of particles by a uniform density implies that the exact overlap energy of a particle within a sphere of radius  $\lambda$  containing a total of  $M$  particles given by  $\varepsilon(M - 1)/2$  is approximated by  $(\varepsilon\rho_{\text{eff}}/2) \int_V \theta(\mathbf{r}) \, dV - \varepsilon/2$ . In this expression, the second term represents the so-called self-energy per particle present in all energies and enthalpies

derived within the continuum model. It is convenient to offset the reduced energy per particle,  $e$ , by the self-energy term and define it by

$$e = \frac{\sigma^3}{\lambda^3} \left( \frac{E}{N\epsilon} + \frac{1}{2} \right) \quad (5)$$

where  $E$  is the energy of all particles within the volume considered. The corresponding reduced enthalpy per particle is

$$h = \frac{\sigma^3}{\lambda^3} \left( \frac{H}{N\epsilon} + \frac{1}{2} \right) = e + \frac{p}{n} \quad (6)$$

where  $H = E + PV$  is the enthalpy,

$$p = \frac{P\sigma^6}{\epsilon\lambda^3} \quad (7)$$

is the reduced pressure, and

$$n = \frac{N\sigma^3}{V} = \rho\sigma^3 \quad (8)$$

is the reduced density. Here,  $N$  and  $V$  are the total number of particles and the volume, respectively. In 2D, these formulas are suitably modified:  $e = \sigma^2(E/N\epsilon + 1/2)/\lambda^2$ ,  $h = \sigma^2(H/N\epsilon + 1/2)/\lambda^2$ ,  $p = P\sigma^4/\epsilon\lambda^2$ , and  $n = N\sigma^2/A = \rho\sigma^2$ , where  $A$  is the area.

## ■ 2D MESOPHASES

Let us first illustrate the workings of the continuum theory by applying it to two-dimensional hard-core/square-shoulder particles where the predictions of the approach can be compared to the results obtained using a range of other methods.<sup>17–19,21,22</sup> The three cluster phases that we compare to the uniform phase (U) are the disk (D), the stripe (S), and the inverted disk morphology (I; Figure 2), all generic to systems with cluster-forming pair interactions<sup>26</sup> which are not limited to repulsive potentials.<sup>27</sup>

**Disk Morphology.** The disk morphology consists of particles arranged into identical circular disks of diameter  $D$  which could form any of the 2D lattices—square, rectangular, oblique, or hexagonal. For simplicity, we only consider the hexagonal lattice, denoting the lattice spacing by  $L$ . Because the particles occupy a part of the plane rather than the whole of it, their effective density within the disks is larger than the average density and reads  $\rho_{\text{eff}} = 2 \cdot 3^{1/2} L^2 \rho / \pi D^2$ . We first evaluate the intradisk overlap energy. In disks smaller than the shoulder width ( $D < \lambda$ ), each particle overlaps with all other particles and the intradisk overlap energy per particle is  $E_{\text{intra}}/N = \epsilon(\pi\rho_{\text{eff}}D^2/4 - 1)/2$ . The calculation of the interdisk energy is somewhat cumbersome because of both the lens-like shape of the overlap zone and the lens-like shape of the subsurface region of the disk that includes the centroids of particles that do overlap with the neighboring disk (Figure 3). Obviously, the overlap zone depends on the position of the particle. The average area of the nearest-neighbor overlap zone can be evaluated numerically, but we stick to an approximate analytical treatment: This demonstrates the most appealing features of the theory much better. The most interesting limit is that of a small disk diameter relative to lattice spacing,  $D < \lambda$ , and partial penetration where the penetration depth defined by

$$\Delta = \lambda + D - L \quad (9)$$

is smaller than the disk diameter  $D$ ,  $\Delta < D$ ;  $\Delta$  represents the largest thickness of the lens-like overlap zone of any particle from

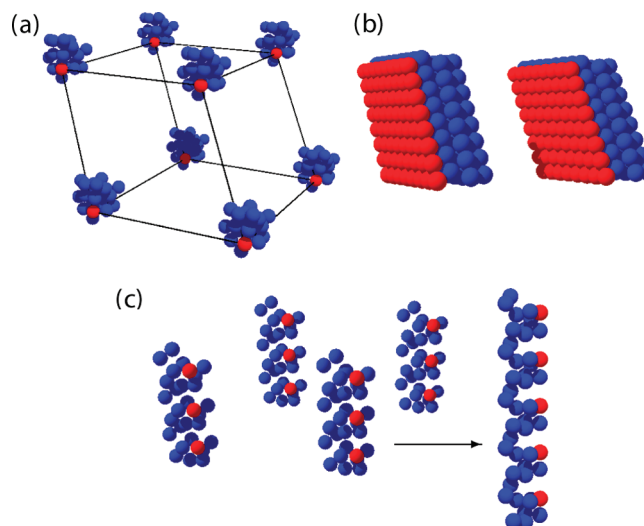


**Figure 1.** Representative examples of spherical (a), lamellar (b), and columnar morphology (c; enlarged is a single column viewed perpendicular to the axis) of a  $\lambda = 10\sigma$  hard-core/square-shoulder system found using genetic algorithms.<sup>25</sup> In all structures, the well-separated compact clusters are clearly visible; the particles at the vertices of the unit cell are colored in red, whereas the additional basis particles are blue. The complete  $T = 0$  phase sequence includes many more minimal-enthalpy configurations:<sup>34</sup> some of them are cluster morphologies, and others are uniform phases of various symmetries.

a disk and a neighboring disk (Figure 3). In this case, the overlap zone is shaped like a thin lens. After averaging over the positions of all particles that do overlap with the neighboring disk, we find that  $E_{\text{inter}}/N = \epsilon\rho_{\text{eff}}\lambda^{3/2}(\lambda + D - L)^3/3DL^{3/2}$ .

The enthalpy per particle includes the energy  $E_{\text{intra}}/N + 6E_{\text{inter}}/N$  (each disk is 6-coordinated) and the pressure term  $P/\rho$ ; in dimensionless form, the enthalpy reads

$$h_{\text{D}}(d, \ell, p, n_{\text{eff}}) = \frac{\pi d^2 n_{\text{eff}}}{8} + \frac{2(1 + d - \ell)^3 n_{\text{eff}}}{d^{3/2}} + \frac{2\sqrt{3}p/\ell^2}{\pi d^2 n_{\text{eff}}} \quad (10)$$

where  $n_{\text{eff}} = \rho_{\text{eff}}\sigma^2$ ,

$$\ell = \frac{L}{\lambda} \quad (11)$$

is the reduced lattice spacing, and

$$d = \frac{D}{\lambda} \quad (12)$$

is the reduced disk diameter. The first two terms in  $h_{\text{D}}(d, \ell, p, n_{\text{eff}})$ —the reduced intra- and intercluster energy, respectively—are proportional to the effective density, whereas the pressure term is inversely proportional to it. The equilibrium reduced density determined by  $\partial h_{\text{D}}(d, \ell, p, n_{\text{eff}})/\partial n_{\text{eff}} = 0$  corresponds to  $\ell = 1$  and  $d = 0$  and reads

$$n_{\text{eq}} = \sqrt{\frac{2\sqrt{3}p/\ell^2}{\pi d^2 [\pi d^2/8 + 2(1 + d - \ell)^3/d^{3/2}]}]} \quad (13)$$

However, the value of  $n_{\text{eq}}$  exceeds the largest possible reduced density of  $n_{\text{max}}^{2\text{D}} = 2/3^{1/2}$  at all pressures (in fact, for  $\ell = 1$  and  $d = 0$ , it diverges), so we conclude that the disks are necessarily close-packed. After substituting  $n = n_{\text{max}}^{2\text{D}}$  into eq 10, we minimize  $h_{\text{D}}(d, \ell, p)$  with respect to  $\ell$  and  $d$  to obtain the equilibrium

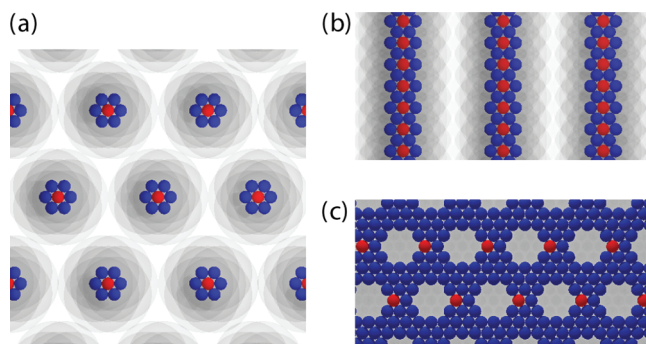


**Figure 2.** Examples of the three 2D cluster phases: disk (a), stripe (b), and inverted disk morphology (c). The solid circles represent the hard cores of the particles, whereas the gray semitransparent circles are the soft coronas; the darker the shade of gray, the more overlapping the coronas. Like in Figure 1, the hard cores of the particles at the vertices of the unit cell are red and the additional basis particles are blue.

reduced lattice spacing

$$\ell = 1 + \sqrt{\frac{2}{\pi}} 3^{3/8} p^{1/4} \left( 1 + \frac{3^{3/8} p^{1/4}}{2\sqrt{2\pi}} \right) - \frac{3^{1/16} p^{3/8}}{2^{3/4} \pi^{1/4}} \left( 1 + \frac{3^{19/8} p^{1/4}}{4\sqrt{2\pi}} \right) \quad (14)$$

and disk size

$$d = \sqrt{\frac{2}{\pi}} 3^{3/8} p^{1/4} \left( 1 + \frac{3^{3/8} p^{1/4}}{2\sqrt{2\pi}} \right) \quad (15)$$

These results are then plugged into  $h_D(d, \ell, p)$  to obtain the enthalpy as an explicit (and remarkably simple) function of pressure

$$h_D(p) = \sqrt{\sqrt{3p}} \left( 1 + \sqrt{\frac{2 \cdot 3^{3/4}}{\pi} \sqrt{p}} \right) \quad (16)$$

**Stripe Morphology.** This is the simplest cluster morphology (Figure 2b): The particles are grouped into equidistant parallel stripes of width  $D$  with the lattice constant  $L$  such that the width of the particle-free gap between the stripes is  $L - D$ . The effective 2D density of particles within the stripes is  $\rho_{\text{eff}} = \rho L/D$ . We assume that the stripe width is smaller than the shoulder range,  $D < \lambda$ , and that the lattice spacing is somewhat larger than the shoulder width,  $L \gtrsim \lambda$ ; these assumptions will be justified *a posteriori* by the predictions of the theory. In this case, the intrastripe energy can be estimated by approximating the overlap zone by a rectangle of width  $D$  and height  $2\lambda$  for any location of the particle. The total number of particles within the overlap zone of volume  $2\lambda D$  is  $2\rho_{\text{eff}}\lambda D$ , and the number of neighbors that any given particle overlaps with is  $2\rho_{\text{eff}}\lambda D - 1$ . The intrastripe overlap energy per particle is then  $E_{\text{intra}}/N \approx \varepsilon(2\rho_{\text{eff}}\lambda D - 1)/2$ . As per the interstripe energy, we have to be a little more careful as the area of the overlap zone depends on the location of the particle within the stripe. The particles within the subsurface region of the stripe will overlap with the particles in the facing stripe; the thickness of the subsurface region is given by the penetration depth  $\Delta = \lambda + D - L$ . For these particles, the overlap

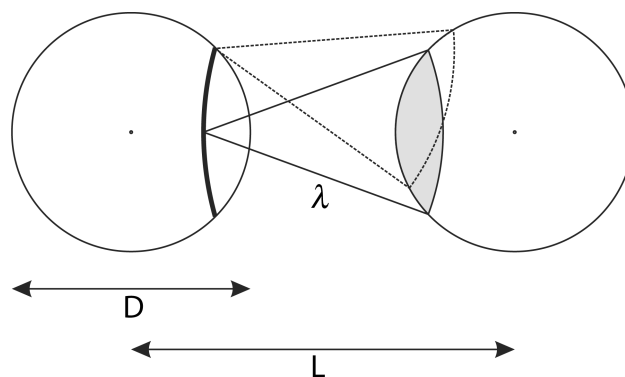


**Figure 3.** Disk-disk interaction: The shaded region represents the lens-shaped overlap zone covered by the shoulder of a particle located within the left disk. The radii of the overlap zone are the shoulder diameter  $\lambda$  and disk radius  $D/2$ ; its thickness depends on the distance of the particle from the center of the right disk and the disk-disk separation  $L$ . The overlap zones of all particles lying within the thick arc-like stripe in the left disk are of identical shape and size.

zone has the shape of a circular cap of radius  $\lambda$  and height  $\lambda + D - L - x$ , where  $x$  is the distance from the particle and the stripe edge, whereas for others it vanishes. The area of the cap is known from elementary geometry, and after integrating over all  $x$  between 0 and  $\Delta$ , we find that to lowest order in  $\Delta$  the average area of overlap zone is  $8 \cdot 2^{1/2} \lambda^{1/2} (\lambda + D - L)^{5/2} / 15D$ . This means that the interstripe overlap energy per particle is  $E_{\text{inter}}/N \approx 4 \cdot 2^{1/2} \varepsilon \rho_{\text{eff}} \lambda^{1/2} (\lambda + D - L)^{5/2} / 15D$ .

Given the average intra- and interstripe overlap energy, we construct the enthalpy per particle  $H/N = E_{\text{intra}}/N + 2E_{\text{inter}}/N + P/\rho = E_{\text{intra}}/N + 2E_{\text{inter}}/N + PL/\rho_{\text{eff}}D$ , where we multiplied the interstripe interaction by a factor of 2 to account for both neighbors of a given stripe. Like for the disk morphology, we can minimize  $H/N$  with respect to  $\rho_{\text{eff}}$ . The result is the same as in the disk phase: The enthalpy is minimal for  $L = \lambda$  and  $D = 0$  which correspond to a diverging equilibrium density which violates the constraint that the effective density does not exceed the 2D close-packing density of  $\rho_{\text{max}}^{2D}$ . We conclude that in equilibrium the stripes are close-packed,  $\rho_{\text{eff}} = \rho_{\text{max}}^{2D}$ .

We now convert the enthalpy per particle into the dimensionless form defined by  $h = \sigma^2(H/N\varepsilon + 1/2)/\lambda^2$ , insert  $n_{\text{eff}} = n_{\text{max}}^{2D}$  from eq 3, and obtain

$$h_S(d, \ell, p) = \frac{2d}{\sqrt{3}} + \frac{16\sqrt{2}}{15\sqrt{3}} \frac{(1 + d - \ell)^{5/2}}{d} + \frac{\sqrt{3}p\ell}{2d} \quad (17)$$

which is then minimized with respect to  $d = D/\lambda$  and  $\ell = L/\lambda$  to find the equilibrium reduced stripe width and lattice constant:

$$d = \sqrt{\frac{3p}{4} \left( 1 - \frac{3^{7/3} p^{2/3}}{40} \right)} \quad (18)$$

and

$$\ell = 1 + \sqrt{\frac{3p}{4} \left( 1 - \frac{3^{7/3} p^{2/3}}{40} \right)} - \frac{3^{4/3} p^{2/3}}{8} \quad (19)$$

These results can be substituted into eq 17 to readily obtain a closed expression for the equilibrium reduced enthalpy of the

stripe morphology:

$$h_s(p) = 2\sqrt{p\left(1 - \frac{3^{7/3}p^{2/3}}{40}\right)} + \frac{\sqrt{3}p}{2} \quad (20)$$

**Inverted Disk Morphology.** The last 2D cluster morphology to be considered is the inverted disk phase, which consists of particles filling the whole plane except for the hexagonal lattice of voids of diameter  $D$  spaced by  $L$  (Figure 2c). The analysis follows the same steps as for disks and stripes. The effective density  $\rho_{\text{eff}} = \rho/(1 - \pi D^2/2 \cdot 3^{1/2}L^2)$  is the average density divided by the fraction of the total area that is occupied by particles. To calculate the average overlap energy, we start with the uniform phase of density  $\rho_{\text{eff}}$  (elaborated below) and then remove the excess particles residing in voids. The total energy of the reference uniform phase is  $E_{\text{ref}} = N'\varepsilon(\pi\rho_{\text{eff}}\lambda^2 - 1)/2$ , where  $N' = N/(1 - \pi D^2/2 \cdot 3^{1/2}L^2)$  is the number of particles including the  $N' - N$  excess particles. Now the total energy of the overlap of the excess particles has to be subtracted, and we do this in two steps. We first imagine that each excess particle is surrounded by a uniform background. Upon its removal, the overlap energy decreases by  $\varepsilon(\pi\rho_{\text{eff}}\lambda^2 - 1)$ . As there are  $N' - N$  excess particles, the total energy is thus reduced by

$$E_{\text{ex}} = (N' - N)\varepsilon(\pi\rho_{\text{eff}}\lambda^2 - 1) \quad (21)$$

However, the excess particles are grouped into voids rather than scattered and those in the same void are separated by less than  $\lambda$ . Thus, the excess particles carry an overlap energy that is smaller than  $E_{\text{ex}}$ : The intra- and intervoid overlap energies

$$E_{\text{intra}} = \frac{(N' - N)\varepsilon\left(\frac{\pi\rho_{\text{eff}}D^2}{4} - 1\right)}{2} \quad (22)$$

and

$$E_{\text{inter}} = \frac{(N' - N)\varepsilon\rho_{\text{eff}}\lambda^{3/2}(\lambda + D - L)^3}{3DL^{3/2}} \quad (23)$$

must not be included. In the evaluation of these terms, we reused the expressions for the average overlap zones calculated for the disk morphology.

In the hexagonal inverted phase, the voids are 6-coordinated and the enthalpy per particle is given by  $H/N = (E_{\text{ref}} - E_{\text{ex}} + E_{\text{intra}} + 6E_{\text{inter}})/N + P/\rho$ . The reduced enthalpy reads

$$\begin{aligned} h_1(d, \ell, p, n_{\text{eff}}) &= \frac{\sqrt{3}\pi\ell^2 - \pi^2d^2 + \pi^2d^4/8 + 2\pi d(1 + d - \ell)^3/\ell^{3/2}}{2\sqrt{3}^{1/2}(1 - \pi d^2/2\sqrt{3}^{1/2})} n_{\text{eff}} \\ &+ \frac{p}{(1 - \pi d^2/2\sqrt{3}^{1/2})n_{\text{eff}}} \quad (24) \end{aligned}$$

The first term represents the overlap energy, and the second one is the pressure term. In the high-density regime which corresponds to small voids and large pressures (specifically, to  $d \ll 1$  and  $\delta = 1 + d - \ell < d$ ), we can derive the equilibrium density and the corresponding enthalpy, and we find that the former reaches the close-packing limit at  $p = 0.4611$  which is just a little below the stripe-inverted disk transition at  $p = 0.4749$  (see below). The immediate conclusion is that the effective reduced density within the inverted disk phase is  $n_{\text{max}}^{2D} = 2/3^{1/2}$  within the whole pressure

range where it is stable. Thus,

$$\begin{aligned} h_1(d, \ell, p) &= \frac{\sqrt{3}\pi\ell^2 - \pi^2d^2 + \pi^2d^4/8 + 2\pi d(1 + d - \ell)^3/\ell^{3/2}}{3^{1/2}(1 - \pi d^2/2\sqrt{3}^{1/2})} \\ &+ \frac{\sqrt{3}p}{2(1 - \pi d^2/2\sqrt{3}^{1/2})} \quad (25) \end{aligned}$$

This result can be minimized only numerically to obtain the equilibrium  $d$  and  $\ell$  as well as the equilibrium reduced enthalpy itself. However, we can use it to analyze the inverted disk-uniform transition: For  $\ell = 1$  and  $d = 0$ , the inverted disk morphology reduces to the uniform phase discussed below and its enthalpy, eq 25, is given by  $\pi/3^{1/2} + 3^{1/2}p/2$  which coincides with  $h_U$  (eq 30). To obtain an approximate expression for the enthalpy of the inverted disk morphology in the vicinity of the transition, we expand eq 25 around  $\ell = 1$  and  $d = 0$ . Solving for equilibrium values of  $d$  and  $\ell$  as functions of pressure close to  $p_t = 2\pi/3$  yields

$$d = \sqrt{\frac{3}{\pi}}\left(\frac{2\pi}{3} - p\right)^{1/2} \left[1 - \frac{\sqrt{3}}{4\sqrt{\pi}}\left(\frac{2\pi}{3} - p\right)^{1/2}\right] \quad (26)$$

and

$$\begin{aligned} \ell &= 1 + \sqrt{\frac{3}{\pi}}\left(\frac{2\pi}{3} - p\right)^{1/2} \left[1 - \frac{\sqrt{3}}{4\sqrt{\pi}}\left(\frac{2\pi}{3} - p\right)^{1/2}\right] \\ &- \frac{3^{1/4}}{2^{3/2}\pi^{1/4}}\left(\frac{2\pi}{3} - p\right)^{3/4} \left[1 + \frac{3\sqrt{3}}{8\sqrt{\pi}}\left(\frac{2\pi}{3} - p\right)^{1/2}\right] \quad (27) \end{aligned}$$

Using these results, we find that close to the inverted disk-uniform transition the enthalpy of the inverted disk morphology can be approximated by

$$h_1(p \lesssim 2\pi/3) = \frac{\pi}{\sqrt{3}} + \frac{\sqrt{3}p}{2} - \frac{3}{4}\left(\frac{2\pi}{3} - p\right)^2 \quad (28)$$

which shows that the transition is continuous.

**Uniform Phase.** In the uniform phase, each particle overlaps with all neighbors lying within its shoulder. The overlap zone is a circle of radius  $\lambda$  and the number of neighbors is  $\pi\rho\lambda^2 - 1$ ; the overlap energy per particle is  $\varepsilon(\pi\rho\lambda^2 - 1)/2$ , and the corresponding enthalpy is  $\varepsilon(\pi\rho\lambda^2 - 1)/2 + P/\rho$ . The enthalpy-minimizing density reads  $(2P/\pi\varepsilon\lambda^2)^{1/2}$  so that the reduced equilibrium density is  $n_{\text{eq}} = (2p/\pi)^{1/2}$ . This result is valid for reduced pressures smaller than  $p_t = 2\pi/3$  where the reduced density reaches the close-packed value of  $n_{\text{max}}^{2D} = 2/3^{1/2}$ . For  $p < p_t$ , the reduced enthalpy per particle is

$$h_U(p < 2\pi/3) = \sqrt{2\pi p} \quad (29)$$

and for  $p > p_t$  where  $n_{\text{eq}} = 2/3^{1/2}$  irrespective of pressure

$$h_U(p > 2\pi/3) = \frac{\pi}{\sqrt{3}} + \frac{\sqrt{3}p}{2} \quad (30)$$

As noted above, the expression describing the enthalpy of the uniform phase below  $p_t$  is irrelevant because the transition from the inverted disks to the uniform phase at  $p_t$  is continuous.

**2D Phase Diagram.** The  $T = 0$  phase sequence of the 2D hard-core/square-shoulder system, predicted by the enthalpies of the candidate morphologies, is with increasing pressure

disks  $\rightarrow$  stripes  $\rightarrow$  inverted disks  $\rightarrow$  uniform phase

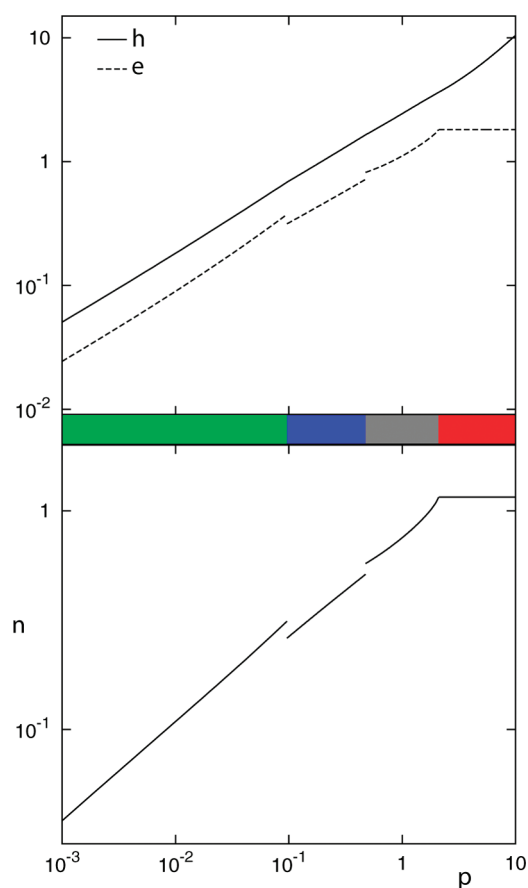


**Figure 4.** Reduced enthalpies and energies (top panel) of the 2D hard-core/square-shoulder cluster morphologies vs reduced pressure. The regions of stability of the various phases are indicated by the color bars separating the panels: green, blue, gray, and red correspond to disk, stripe, inverted disk, and uniform morphology, respectively. The disk–stripe transition occurs at  $p_{D-S} = 0.096$ , and the transition from stripes to inverted disks is at  $p_{S-I} = 0.475$ ; note that these transitions are discontinuous. The transition from inverted disk morphology to uniform phase at  $p_{I-U} = 2\pi/3 \approx 2.094$  is continuous. Bottom panel: Equilibrium reduced density as a function of  $p$ .

Figure 4 shows that the disk–stripe and the stripe–inverted disk transition are discontinuous, whereas the inverted disk–uniform transition is continuous. The phase transition pressures read  $p_{D-S} = 0.096$ ,  $p_{S-I} = 0.475$ , and  $p_{I-U} = 2.094$ . These values can be compared to the transition pressures in exact MEC structures found by the genetic algorithm approach.<sup>22,23,28</sup> The scope of the comparison is limited because the exact MEC structures cannot capture the inverted morphology.<sup>29</sup> Nonetheless, for large  $\lambda/\sigma$ —this is the regime where the continuum model is expected to perform well—the agreement is reasonable. For  $\lambda/\sigma = 10$ , the genetic-algorithm MECs put the disk–stripe transition at  $p = 0.0042$ ,<sup>23,28</sup> which is an order of magnitude below our value for  $p_{D-S}$ . On the other hand, the stripe–uniform transition predicted by MECs obtained by the genetic algorithm search is at  $p = 0.639$ <sup>23,28</sup> which is somewhat above our  $p_{S-I}$ . However, one can imagine that if the exact MEC phase sequence did include the inverted morphology the genetic algorithm minimization would push the stripe–inverted transition to a pressure smaller than 0.639 and thus closer to our prediction. Given the approximations inherent to the continuum model, we can be reasonably satisfied with this agreement.

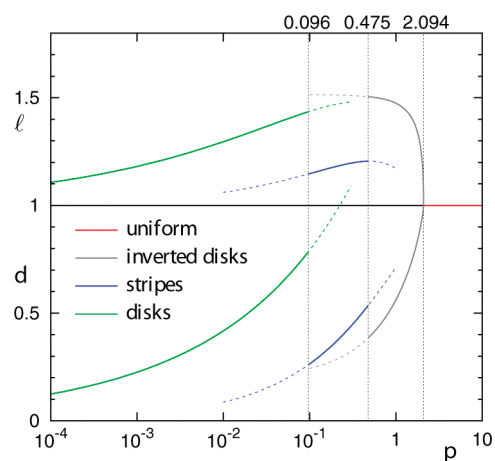


**Figure 5.** Structural parameters of the 2D cluster morphologies as functions of pressure; solid and dashed lines correspond to equilibrium and metastable states, respectively, and top labels indicate the phase transition pressures. In the disk and the stripe morphology, the lattice spacing (top part of the figure) increases with pressure, whereas, in the inverted disk morphology, it is gradually decreased upon compression until it reaches 1 at the transition to uniform phase at  $p_{I-U} = 2.094$ . The bottom part of the figure shows the cluster size defined by  $d$  in the disk and the stripe morphology and by  $l - d$  in the inverted disk morphology. The cluster size is an increasing function of pressure in all phases, which is expected. The uniform phase can be regarded as the inverted disk morphology with  $l = 1$  and  $l - d = 1$ , and is represented by the red horizontal section at pressures larger than  $p_{I-U}$ .

Let us look at the behavior of the structural parameter of the disk, stripe, and inverted disk cluster morphologies (Figure 5). Across all phases, the lattice spacing is somewhat larger than  $\lambda$ —its average value is close to  $\approx 1.2\lambda$  consistent with the lattice theory and the results of Monte Carlo simulations.<sup>21</sup> This justifies the assumption made in the analysis where we presupposed that  $l \gtrsim 1$ . The size of clusters is encoded in the disk diameter, stripe thickness, and thickness of the inverted disk morphology defined as the difference between the lattice spacing and void diameter. In all cluster morphologies, the cluster size is an increasing function of pressure, which is expected. The behavior of the structural parameters in the inverted morphology provides another illustration of the continuity of the inverted disk–uniform phase transition: As  $p$  approaches  $p_{I-U}$ , both  $l$  and  $l - d$  approach 1 which represents the void-free uniform phase. Note that in the disk and stripe morphologies  $d < 1$  and  $\delta = 1 + d - l < d$  as anticipated in the approximate analysis.

Another point to note is that in all cluster morphologies the particles are close-packed and their effective intracluster reduced density is  $n_{\text{max}}^{2D} = 2/3^{1/2}$ . In addition, the transition from the inverted disks to the uniform phase takes place at  $p = 2\pi/3$  where the latter becomes close-packed as discussed above—so that the stable uniform phase is close-packed too. This detail has been mentioned when discussing each of the cluster morphologies, but we emphasize it again because it is a common feature of all phases. A different way of putting it would be to say that, in equilibrium, the separation of the voids and the clusters is as complete as possible. Thus, the clusters behave as if they were held together by an effective surface tension, which is a collective rather than pairwise effect because the pairwise interaction is repulsive. Conceptually, the effective surface tension is helpful in understanding why the geometry of the cluster phases is the same as that in, say, diblock copolymer melts where the microscopic

interactions can be more directly associated with a positive surface tension.<sup>30</sup>

### 3D MESOPHASES

The above results offer a clear insight into the mechanism of clustering, but their relevance for experimental systems is limited to particles confined to a thin cell<sup>31</sup> or an interface.<sup>32</sup> The 3D case is considerably more appealing and potentially useful because it covers some aspects of the phase behavior of dense suspensions of dendrimer-based self-organized nanocolloids<sup>33</sup> and related systems. We consider the spherical (S), columnar (C), lamellar (L), inverted columnar (IC), and inverted spherical morphology (IS) as well as the uniform phase (U).

**Spherical Morphology.** We begin with spherical clusters and consider spheres on three cubic lattices with a single type of sites — the face centered cubic (FCC), the body centered cubic (BCC), and the simple cubic (SC) lattice. In all three lattices, the relation between the effective number density within clusters and the actual number density can be written as  $\rho_{\text{eff}} = \rho L^3 / fD^3$ , where  $f$  is the packing fraction of each lattice:  $f = 2^{1/2}\pi/6 \approx 0.740$  in FCC lattice;  $f = 3^{1/2}\pi/8 \approx 0.680$  in BCC lattice; and  $f = \pi/6 \approx 0.524$  in SC lattice. We first calculate the average intracolumnar overlap energy. As the sphere diameter  $D$  is assumed to be smaller than the shoulder width, the overlap zone is the whole sphere itself and  $E_{\text{intra}}/N = \varepsilon(\pi\rho_{\text{eff}}D^3/6 - 1)/2$  in all lattices in question. For  $D$  sufficiently smaller than  $\lambda$ , the average interaction of a particle with particles in a neighboring sphere can be well approximated by replacing the exact biconvex lens-shaped overlap zone of radii  $D/2$  and  $\lambda$  by a spherical cap of radius  $D/2$  and identical thickness. After averaging over the position of the particle within the spherical cluster, we obtain  $E_{\text{inter}}/N = \pi\varepsilon\rho_{\text{eff}}(\lambda + D - L)^4[(\lambda - 2D - L)^2 - 3D^2/2]/60D^3$ . The total overlap energy of a sphere with its neighbors is  $kE_{\text{inter}}/N$ , where  $k$  is the number of nearest neighbors (12, 8, and 6 in the FCC, BCC, and SC lattice, respectively).

The pressure term is given by  $P/\rho = L^3P/fD^3\rho_{\text{eff}}$  and like in 2D, an inspection of the enthalpy  $H/N = E_{\text{intra}}/N + kE_{\text{inter}}/N + P/\rho$  shows that the equilibrium configuration corresponds to close-packed clusters which is consistent with the compactness of the spherical MECs found using genetic algorithms.<sup>25,34</sup> After substituting  $\rho_{\text{eff}}$  by  $\rho_{\text{max}}^{3D} = 2^{1/2}/\sigma^3$  and switching to dimensionless quantities, the reduced enthalpy reads

$$h_S(d, \ell, p) = \frac{\sqrt{2}\pi}{12} d^3 + k \frac{\sqrt{2}\pi}{60} \frac{(1 + d - \ell)^4 [(1 - 2d - \ell)^2 - 3d^2/2]}{d^3} + \frac{8p}{\sqrt{2}f} \frac{\ell^3}{d^3} \quad (31)$$

where  $d = D/\lambda$  and  $\ell = L/\lambda$  are the reduced sphere diameter and lattice spacing, respectively. For lattice spacing larger than the disk diameter ( $\ell/d > 1$ ) and penetration depths not exceeding 25% of the disk diameter ( $\delta/d = \Delta/D \lesssim 0.25$ ; this covers the pressure range where the spherical morphologies are stable),  $h_S$  can be somewhat simplified and finally minimized with respect to  $d$  and  $\ell$  in a semianalytic fashion.<sup>34</sup> We will return to the pressure dependence of the lattice spacing in the discussion of the phase diagram; at this point, let us just note that in all three lattices the equilibrium reduced sphere radius increases roughly as  $p^{0.176}$  from about 0.12 at  $p = 10^{-6}$  to about 0.6 at  $p = 10^{-2}$ . In the following, we show that the spherical morphologies are stable at

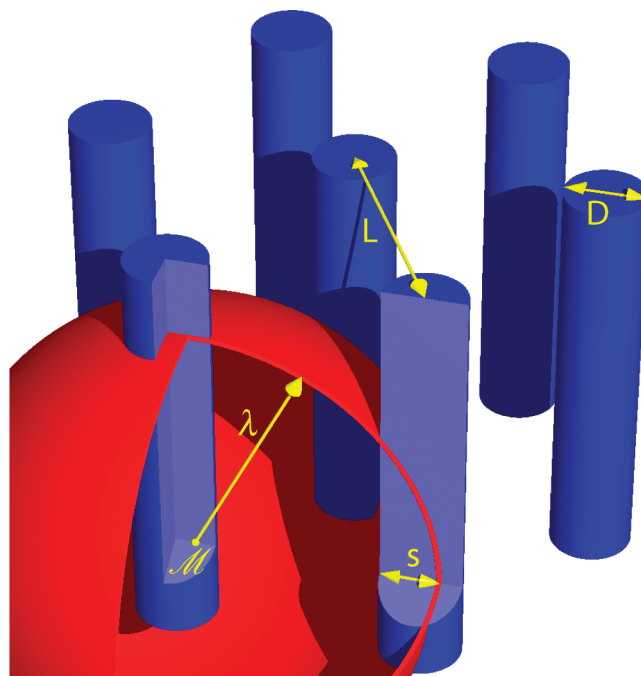


**Figure 6.** Geometry of the hexagonal columnar morphology, which consists of parallel cylinders of diameter  $D$  separated by  $L$ . The shoulder potential of a particle at  $\mathcal{M}$  (red sphere of radius  $\lambda$ ) defines the intracolumnar overlap zone which is, to a good approximation, a cylinder of height  $2\lambda$  and diameter  $D$  irrespective of the location of  $\mathcal{M}$  within the column. The shape of the intercolumnar overlap zone—a cross section of a sphere and a cylinder—is of a somewhat more complicated shape. Its thickness measured radially relative to  $\mathcal{M}$  in the horizontal plane and indicated by  $s$  depends on the location of  $\mathcal{M}$  and ranges from 0 to the penetration depth  $\Delta$ , the latter corresponding to those points on the column surface that directly face the neighboring column.

pressures up to  $p = 0.013$  so that the diameter of the spheres remains smaller than the shoulder width up to the transition to the cylindrical morphology.

**Columnar Morphology.** Like spheres, cylinders can also be arranged in various ways: They may form a hexagonal, oblique, rhombic, rectangular, or square lattice. We restrict the discussion to the hexagonal lattice (Figure 6) as the most common type of columnar morphology in related self-assembled systems such as diblock copolymers<sup>35</sup> and amphiphile solutions.<sup>15</sup> The effective number density of particles arranged in cylindrical columns of diameter  $D$  separated by  $L$  is  $\rho_{\text{eff}} = 2 \cdot 3^{1/2} L^2 \rho / \pi D^2$ —the conversion factor is the ratio of the areas of the 2D unit cell of the hexagonal lattice ( $3^{1/2}L^2/2$ ) and the cross section of a column ( $\pi D^2/4$ ). In the evaluation of the intra- and intercolumnar energies, we focus on cylinders narrower than the shoulder width ( $D < \lambda$ ). We also assume that the penetration depth  $\Delta$  defined by eq 9 is smaller than the diameter of the cylinders,  $\Delta < D$ . In this limit, the intracolumnar overlap zone is a cylinder of diameter  $D$  and height  $2\lambda$  so that, to lowest order, the associated energy per particle reads  $E_{\text{intra}}/N \approx \varepsilon(\pi\rho_{\text{eff}}\lambda D^2/2 - 1)/2$ . The closed-form expression for the intercolumnar overlap energy is much more complicated, the reason being the shape of the overlap zone which is an off-center cross section of a large sphere and a thin cylinder. The result can be expressed using elliptic integrals,<sup>36</sup> but it is a bit too awkward for our purpose. Instead, we derive an approximate formula valid for  $\Delta \lesssim D/2$ . In this case,  $E_{\text{inter}}/N \approx 32 \cdot 2^{1/2} \varepsilon \rho_{\text{eff}} \lambda^{1/2} (\lambda + D - L)^{7/2} / 175D$ .

The analysis of the equilibrium effective density again indicates that  $\rho_{\text{eff}} = \rho_{\text{max}}^{3\text{D}}$ . By combining  $E_{\text{intra}}/N$  and  $6E_{\text{inter}}/N$  (each column has six nearest neighbors) with the pressure term  $P/\rho$  and rewriting the result in reduced units, we arrive at an approximate expression for the reduced enthalpy as a function of reduced cylinder radius  $d = D/\lambda$ , reduced lattice spacing  $l = L/\lambda$ , and reduced pressure

$$h_{\text{C}}(d, l, p) = \frac{\sqrt{2\pi}d^2}{4} + \frac{384}{175} \frac{(1 + d - l)^{7/2}}{d} + \frac{\sqrt{6}}{\pi} \frac{p/l^2}{d^2} \quad (32)$$

The equilibrium values of the two structural parameters can only be found numerically, and after that, the reduced enthalpy can be computed as a function of pressure alone. An inspection of the equilibrium  $d$  and  $\delta = \Delta/\lambda$  shows that both increase with reduced pressure, reaching their respective maximal values of 0.70 and 0.46 at the columnar-lamellar transition at  $p \approx 0.39$  (below we discuss the structural parameters and the phase diagram in more detail). This means that  $\delta/d < 0.66$  so that both assumptions made in the above analysis ( $d < 1$  and  $\delta/d < 1$ ) are justified *a posteriori*.

**Lamellar Morphology.** In the lamellar morphology, the centers of the particles are confined to equidistant parallel slabs of thickness  $D$  whose lattice constant is  $L$ ; like in the 2D stripe phase, the effective number density within the lamellae is  $\rho_{\text{eff}} = L\rho/D$ . For this simple density profile, it is possible to evaluate the overlap energy in closed form but the results are not very transparent.<sup>34</sup> However, the results obtained using genetic algorithms<sup>24,25</sup> suggest that the stable lamellae are narrower than the shoulder width,  $D < \lambda$ , and their lattice constant is somewhat larger than the shoulder width,  $L \gtrsim \lambda$ . Thus, we focus on this regime where the overlap energy reduces to a tractable formula.

To lowest order in  $D/\lambda$ , the intralamellar overlap zone of a particle is a flat cylindrical disk of radius  $\lambda$  and thickness  $D$  irrespective of the location of the particle. In this case,  $E_{\text{intra}}/N \approx \varepsilon(\pi\rho_{\text{eff}}\lambda^2D - 1)/2$ . The overlap zone of the interlamellar term is a spherical cap of radius  $\lambda$  because we assume that  $L$  is larger than  $\lambda$  (yet of comparable magnitude). Its height is largest for particles facing the neighboring lamella and vanishes in those outside the subsurface layer. To lowest order,  $E_{\text{inter}}/N = \pi\varepsilon\rho_{\text{eff}}\lambda(\lambda + D - L)^3/6D$ . To construct the enthalpy, we need to combine  $E_{\text{intra}}/N + 2E_{\text{inter}}/N$  (each lamella interacts with two neighbors) with the pressure term per particle which reads  $P/\rho = PL/\rho_{\text{eff}}D$ .

Like in all other cluster morphologies, we find that the optimal lamellae are closely packed with particles,  $\rho_{\text{eff}} = \rho_{\text{max}}^{3\text{D}}$ . Upon minimizing the enthalpy, we obtain the equilibrium lamellae thickness  $D$  and lattice constant  $L$ . In reduced units  $d = D/\lambda$  and  $l = L/\lambda$ , they read

$$d = \sqrt{\frac{p}{\pi} \left(1 - \sqrt{2p/9\pi}\right)} \quad (33)$$

and

$$l = 1 + \sqrt{\frac{p}{\pi} \left(1 - \sqrt{2p/9\pi}\right)} - \sqrt{\frac{p}{2\pi}} \quad (34)$$

respectively. Using these results, the reduced enthalpy per particle can be written in a compact form:

$$h_{\text{L}}(p) = \sqrt{2\pi p \left(1 - \sqrt{2p/9\pi}\right)} + \frac{p}{\sqrt{2}} \quad (35)$$

Before proceeding, let us quantify the penetration of shoulders of particles within a given lamella into the neighboring lamellae.

Given  $d(p)$  and  $l(p)$  (eqs 33 and 34), we can calculate the reduced penetration depth  $\delta = \Delta/\lambda$  and compare it to reduced lamellae thickness

$$\frac{\delta}{d} = \sqrt{2 \left(1 - \sqrt{\frac{2p}{9\pi}}\right)}^{-1} \quad (36)$$

which is smaller than 1 for all  $p < 9\pi/8 \approx 3.53$ . As shown below, the range of stability of the lamellar phase is well within this limit so that the soft-repulsion shoulders of particles penetrate into but do not protrude through the neighboring lamellae. This also means that each lamella only interacts with its nearest neighbors. A similar albeit less transparent analysis can be done for other morphologies, and in all of them, nearest-neighbor clusters penetrate into but do not protrude through each other.

**Inverted Columnar Morphology.** The inverted columnar morphology is the 3D variant of the inverted disk phase; again, we restrict the discussion to the hexagonal arrangement of cylindrical voids. The effective density is the same as in the inverted disk phase:  $\rho_{\text{eff}} = \rho/(1 - \pi D^2/2 \cdot 3^{1/2}L^2)$ , where  $D$  is the void diameter and  $L$  is the lattice spacing. The total energy of the reference uniform phase is  $E_{\text{ref}} = N'\varepsilon(4\pi\rho_{\text{eff}}\lambda^3/3 - 1)/2$ , where  $N' = N/(1 - \pi D^2/2 \cdot 3^{1/2}L^2)$ . The overlap energy of each excess particle in a uniform background is  $\varepsilon(4\pi\rho_{\text{eff}}\lambda^3/3 - 1)$  so that the total overlap energy of  $N' - N$  excess particles reads  $E_{\text{ex}} = (N' - N)\varepsilon(4\pi\rho_{\text{eff}}\lambda^3/3 - 1)$ . If we assume that the penetration depth  $\Delta$  is much smaller than the void diameter  $D$  and that  $D$  is smaller than the shoulder width  $\lambda$ , the intravoid energy is  $E_{\text{intra}} = (N' - N)\varepsilon(\pi\rho_{\text{eff}}D^2\lambda/2 - 1)/2$  and the intervoid energy is  $E_{\text{inter}} = 32 \cdot 2^{1/2}(N' - N)\varepsilon\rho_{\text{eff}}\lambda^{1/2}(\lambda + D - L)^{7/2}/175D$ .

In the inverted columnar morphology, the enthalpy per particle is given by  $H/N = (E_{\text{re}} - E_{\text{ex}} + E_{\text{intra}} + 6E_{\text{inter}})/N + P/\rho$ . Upon rewriting  $H/N$  in reduced units and replacing the effective reduced density  $n_{\text{eff}}$  by the reduced close-packed density of  $2^{1/2}$  (which is motivated by the behavior of the other cluster phases and by the results of the analysis of MECs using genetic algorithms), we obtain

$$h_{\text{IC}}(d, l, p) = \frac{4\pi l^2/\sqrt{3} - 4\pi^2 d^2/3 + \pi^2 d^4/4 + 192\pi d(1 + d - l)^{7/2}/175}{\sqrt{6}l^2(1 - \pi d^2/2\sqrt{3}l^2)} + \frac{p}{\sqrt{2}(1 - \pi d^2/2\sqrt{3}l^2)} \quad (37)$$

**Inverted Spherical Morphology.** The analysis of the inverted spherical morphology closely follows those of spherical clusters and the inverted columns. The three lattices considered are FCC, BCC, and SC with  $k = 12, 8,$  and  $6$  nearest neighbors, respectively. The effective density reads  $\rho_{\text{eff}} = \rho/(1 - fD^3/L^3)$ , where  $f$  is the packing fraction introduced in the discussion of the spherical morphology;  $D$  and  $L$  are the void diameter and the lattice spacing, respectively. The total energy of the reference uniform phase,  $E_{\text{ref}} = N'\varepsilon(4\pi\rho_{\text{eff}}\lambda^3/3 - 1)/2$ , and the total overlap energy of  $N' - N$  isolated excess particles in a uniform phase,  $E_{\text{ex}} = (N' - N)\varepsilon(4\pi\rho_{\text{eff}}\lambda^3/3 - 1)$ , are essentially the same as in the inverted columnar morphology except that the number of excess particles  $N'$  is given by  $N/(1 - fD^3/L^3)$ . If one assumes that the void diameter is smaller than the shoulder width,  $D < \lambda$ , the intravoid energy reads  $E_{\text{intra}} = (N' - N)\varepsilon(\pi\rho_{\text{eff}}D^3/6 - 1)/2$

and the intervold energy is  $E_{\text{inter}} = (N' - N)\epsilon\rho_{\text{eff}}(\lambda + D - L)^4/8D$ ; the latter describes the limited penetration regime  $\Delta \ll D$ .

The enthalpy per particle of the inverted spherical morphology is  $H/N = (E_{\text{ref}} - E_{\text{ex}} + E_{\text{intra}} + kE_{\text{inter}})/N + P/\rho$ , where  $k$  is the number of nearest neighbors. Again, we recast  $H/N$  in reduced units and insert  $n_{\text{eff}} = 2^{1/2}$  using the same arguments as in the inverted columnar morphology. Thus, we arrive at

$$h_{\text{IS}}(d, \ell, p, n_{\text{eff}}) = \sqrt{2} \frac{2\pi\ell^3/3 - 4\pi fd^3/3 + \pi fd^6/12 + kfd^2(1+d-\ell)^4/8}{\ell^3(1-fd^3/\ell^3)} + \frac{p}{\sqrt{2}(1-fd^3/\ell^3)} \quad (38)$$

As discussed below, eqs 37 and 38 are not as useful as one would like because the approximate analysis presented here predicts stable inverted phases outside the respective regimes of validity for the approximations made.

**Uniform Phase.** Like in 2D, the energy of a particle in the uniform phase consists of the overlaps of its shoulder with all neighbors within a sphere of radius  $\lambda$ :  $\epsilon(2\pi\rho\lambda^3/3 - 1)/2$  and the enthalpy per particle reads  $\epsilon(2\pi\rho\lambda^3/3 - 1)/2 + P/\rho$ . The equilibrium effective density is  $(3P/2\pi\epsilon\lambda^3)^{1/2}$  provided that the pressure is smaller than  $P_t = 4\pi\lambda^3\epsilon/3\sigma^6$ . At  $P_t$ , the density reaches the close-packed density  $\rho_{\text{max}}^{3\text{D}} = 2^{1/2}/\sigma^3$ .

By inserting the equilibrium density into the enthalpy and translating it into reduced units, we find that for reduced pressures below the threshold of  $p_t = 4\pi/3$

$$h_{\text{U}}(p < 4\pi/3) = \sqrt{\frac{8\pi p}{3}} \quad (39)$$

whereas beyond the threshold pressure

$$h_{\text{U}}(p > 4\pi/3) = \frac{2\sqrt{2}\pi}{3} + \frac{p}{\sqrt{2}} \quad (40)$$

**Phase Diagram.** The above results give the enthalpy of the candidate morphologies either directly in terms of a closed-form expression (lamellar morphology and uniform phase) or indirectly after minimization with respect to cluster size and spacing (columnar and spherical morphologies as well as their inverted counterparts). By comparing the enthalpies, we can construct the  $T = 0$  phase diagram of the 3D hard-core/square-shoulder system. However, the approximate expressions for the enthalpies of the inverted morphologies (eqs 37 and 38 where we assume that the void diameter is smaller than the shoulder width) underestimate the actual  $h_{\text{IC}}$  and  $h_{\text{IS}}$ —to the extent that they seem to be stable outside the validity regime of the approximations made. Only after we replace the approximate formulas by the exact expressions and minimize the latter with respect to the structural parameters do all the morphologies appear in the phase sequence which reads with increasing pressure

spheres  $\rightarrow$  columns  $\rightarrow$  lamellae  $\rightarrow$  inverted columns  
 $\rightarrow$  inverted spheres  $\rightarrow$  uniform phase

the reduced pressures of the five transitions being  $p_{\text{S-C}} \approx 0.00857$ ,  $p_{\text{C-L}} \approx 0.0516$ ,  $p_{\text{L-IC}} \approx 3.41$ ,  $p_{\text{IC-IS}} \approx 3.89$ , and  $p_{\text{IS-U}} = 4\pi/3 \approx 4.19$ , respectively (Figure 7). The only stable spherical and inverted spherical morphology is the FCC lattice, but we note that the enthalpy of the BCC lattice is typically not

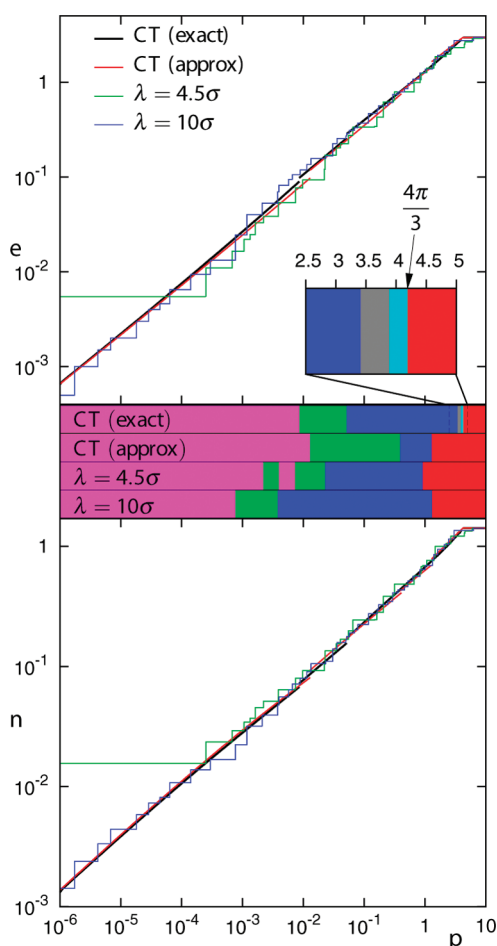


**Figure 7.** Reduced energy (top panel) and reduced density (bottom panel) of the cluster morphologies and the uniform phase obtained by the exact and the approximate continuum theory (black and red lines, respectively) and by the genetic algorithm approach for  $\lambda = 4.5\sigma$  and  $\lambda = 10\sigma$  (jagged green and blue lines, respectively). The set of MECs identified by the genetic algorithm approach is discrete, and this is why the corresponding profiles of  $e$  and  $n$  are step-like; apart from that, the agreement is good except at very small pressures where the finite shoulder-to-core ratio causes an expected deviation of the continuum model from the discrete genetic algorithm MECs. The magenta/green/blue/gray/cyan/red bars separating the panels indicate the ranges of stability of the spherical/columnar/lamellar/inverted columnar/inverted spherical/uniform morphologies obtained by the two variants of the continuum model and the two sequences of MECs identified using the genetic algorithm. The only approach which does predict the inverted morphologies is the exact continuum model.

much larger. For example, the relative difference of the BCC and FCC enthalpies obtained within the approximate continuum model is a decreasing function of pressure which does not exceed 5% and amounts to 2.4% at the transition from the FCC spherical to the columnar morphology. Like in 2D, the transition from inverted spheres to the uniform phase takes place at a pressure beyond which the latter is close-packed.

The only qualitative difference between the phase sequence predicted by the continuum model and that obtained by the low-temperature limit of the lattice theory<sup>37</sup> is the symmetry of the spherical and the inverted spherical morphologies: In our analysis, the stable variants of these two morphologies are FCC lattices rather than BCC lattices as found in ref 37. However, in

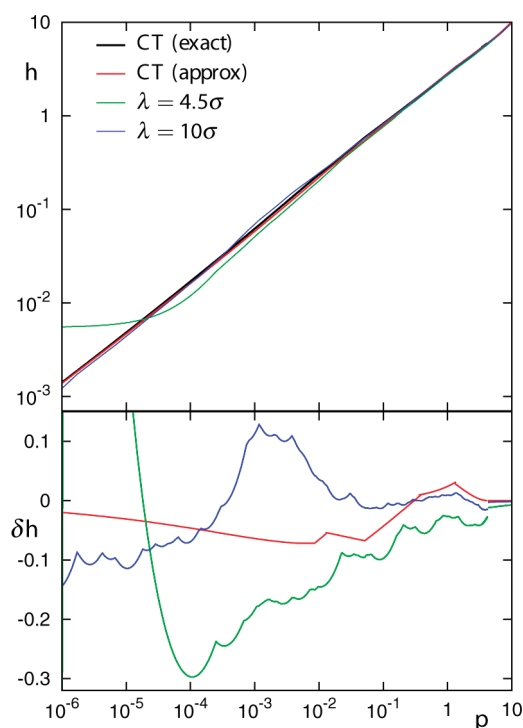


**Figure 8.** Enthalpy of the cluster morphologies and the uniform phase as a function of pressure (top panel): The predictions of the exact and the approximate continuum model (black and red lines, respectively) vs MEC results for  $\lambda = 4.5\sigma$  and  $10\sigma$  obtained using genetic algorithms (green and blue lines, respectively). The agreement of all approaches is generally very good: The bottom panel shows the relative deviation of the approximate continuum model, the  $\lambda = 4.5\sigma$ , and the  $10\sigma$  MECs (red, green, and blue lines, respectively) from the exact continuum model. More precisely,  $\delta h = h/h_{CT,ex} - 1$ , where  $h$  is the enthalpy of any of the three results being compared to the enthalpy of the exact continuum model  $h_{CT,ex}$ . The pressure range shown spans across all of the cluster morphologies and the uniform phase, yet the slope of any of the curves in the top panel does not change much. The only exception is the  $\lambda = 4.5\sigma$  curve at small pressures; at even lower pressures than those shown here, the same happens to the  $\lambda = 10\sigma$  curve. This suggests that the phase transition pressures are quite sensitive to any approximations used in the analysis.

view of the small differences of the enthalpies of FCC and BCC spherical morphologies discussed above, the discrepancy does not seem very important. Given the approximations made with the continuous distribution  $\theta(\mathbf{r})$  (see eq 2), we can conclude that the agreement of the predictions of the two complementary methods is quite good.

By converting the reduced transition pressures into actual shoulder-specific values, i.e.,  $P = \varepsilon\lambda^3 p/\sigma^6$ , the universal transition points can be translated into the phase diagram for any shoulder-to-core ratio  $\lambda/\sigma$ , and they are expected to describe it reasonably well provided that the ratio is larger than 1, say 3 or more. At this juncture, we compare them with the minimal-enthalpy structures found by the genetic algorithm search.<sup>24,25</sup> Figure 7 shows the total overlap energy and the density of the three cluster morphologies and the uniform phase calculated using the continuum theory as well as the  $\lambda = 10\sigma$  and  $\lambda = 4.5\sigma$  MECs obtained by the genetic algorithm approach. As expected, the latter predict a stairway-like, piecewise-constant energy and density profiles but the agreement with the predictions of the continuum theory is surprisingly good across a broad pressure range spanning several

orders of magnitude, and this applies equally well to both  $\lambda = 4.5\sigma$  and  $\lambda = 10\sigma$ . This suggests that, as far as the enthalpy itself is concerned, the continuum theory performs very well for shoulders broader than about  $5\sigma$ .

However, the good agreement of the enthalpies obtained by the two approaches does not guarantee that the phase transitions themselves will coincide. The exact continuum-model enthalpies of any two morphologies intersect at an acute angle (Figure 8) so that the phase transition pressures are rather sensitive to the precise values of enthalpies computed using the approximations mentioned above which, albeit reasonable, introduce certain inaccuracies. As shown in Figure 8, the relative deviation of the approximate and the exact analyses does not exceed 7%. At large pressures where the inverted morphologies are stable, the difference is far smaller—but the approximate theory cannot describe the inverted phases self-consistently. The enthalpies of the genetic-algorithm MECs depart from the exact continuum theory somewhat more than its approximate variant but not dramatically (except at very small pressures where the continuum theory is not applicable anyhow). Generally speaking, the agreement is better at large pressures which is reasonable because in this regime the occupancy of the clusters is large. As expected, the larger the ratio of shoulder-to-core diameter, the smaller the deviation.

Despite the reasonably good agreement of the enthalpies, the phase transition pressures computed using the two variants of the continuum model as well as the genetic-algorithm MEC structures are quite different. In our view, the main reason for this is not the nature of the methods used itself but the very acute intersections of the adjacent sections of the enthalpies. This seems to be an intrinsic property of the hard-core/square-shoulder system. In addition, the mismatch of the phase transition pressures may be due to the complex structure of the spherical and columnar morphologies that were found using genetic algorithms.<sup>34</sup> Unlike the lamellar morphologies, which typically consist of no more than a few basis particles in a very elongated unit cell—as a rule of thumb, the side ratio is 10:1:1—the spherical and columnar clusters comprise many more particles which makes their identification more complicated. Moreover, many of the columnar clusters found are characterized by an intricate internal structure as opposed to the equally large but typically much more compact spherical clusters. As a result, the columnar morphologies are the least robust cluster morphology. In view of the very similar enthalpy profiles, it is not hard to imagine that it may be partly overridden by the more robust spherical and lamellar morphologies, which puts the quantitative differences between the phase sequences shown in Figure 8 in a more realistic perspective. We note that discrepancies of similar nature and magnitude are observed when the continuum theory is compared to Monte Carlo simulations.<sup>21</sup>

Finally, we turn to the two structural parameters of the cluster morphologies. Figure 9 shows the lattice spacing  $\ell$  and the cluster size  $d$  of all morphologies computed using the exact continuum model as functions of pressure; in the inverted morphologies, cluster size is defined as  $\ell - d$  which corresponds to the smallest thickness of the wall that separates the neighboring voids. The overall profile of the lattice spacing is very similar to that seen in the 2D hard-core/square-shoulder system (Figure 5). In the spherical and columnar morphology, it gradually increases with pressure and so does the cluster size. In the lamellar morphology, the lattice spacing is virtually constant across a pressure range spanning almost 2 decades, whereas the lamellae thickness

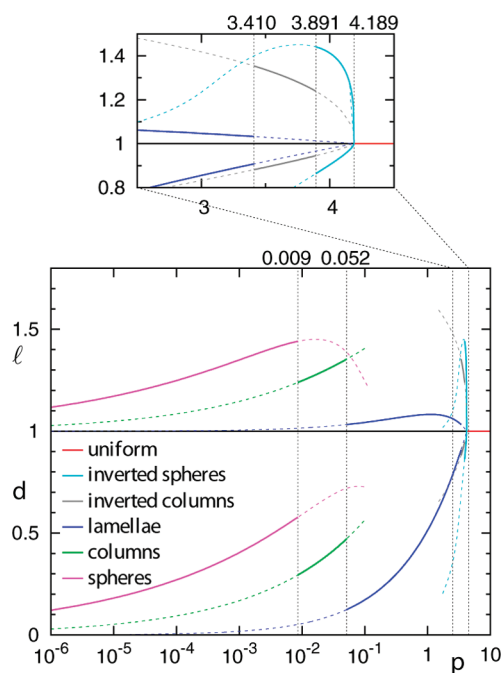


**Figure 9.** Lattice spacing and cluster size as a function of reduced pressure for spherical, columnar, lamellar, and the two inverted 3D morphologies; solid and dashed sections refer to stable and metastable regimes, respectively, and the structural parameters of the inverted morphologies are shown in the expanded part of the diagram. The phase transitions are indicated by the vertical dotted lines labeled by the corresponding pressures. The pressure dependence of the lattice spacing is rather weak in all morphologies except in the inverted spheres which undergo a continuous transition to the uniform phase at  $p_{IS-U} = 4.189$  (represented by the red horizontal segment at  $p > p_{IS-U}$ ). On the other hand, the cluster size does increase steadily with pressure, especially in the lamellar morphology. Qualitatively, the behavior of both  $l$  and  $d$  is very similar to that observed in the 2D hard-core/square-shoulder system (Figure 5).

increases considerably. The inverted morphologies are marked by monotonically decreasing lattice spacing accompanied by ever smaller voids. The overall variation of  $l$  with pressure is more pronounced than in the 2D case yet small given the pressure range in question. This remarkable property of the hard-core/square-shoulder systems has been observed earlier in a 2D system,<sup>21</sup> and Figure 9 demonstrates that it also applies to the 3D ensemble. Apart from this, the numerical values of the lattice spacing and cluster size obtained with the exact continuum model justify *a posteriori* the approximations made in the calculations of the overlap energies in the spherical, columnar, and lamellar morphology.

The two structural parameters discussed in Figure 9 also illustrate the limit of validity of the continuum theory. Consider the spherical morphology stable in the low-pressure regime: As  $p$  is decreased, the diameter of the spherical clusters becomes small compared to the shoulder width which suggests that the clusters themselves gradually lose their meaning because they only include a small number of particles. This violates the basic assumption of the continuum theory—it relies on the existence of compact clusters large enough so that the intracenter density profile can be considered uniform. This is obviously not fulfilled in small clusters containing no more than a few particles, which cannot be described consistently using continuum theory. The

limit of its applicability depends on the shoulder-to-core ratio  $\lambda/\sigma$ , and there is no universal cutoff to curb the validity of the continuum theory. Particles with very large  $\lambda/\sigma$  will satisfy the above condition in clusters whose size may be small compared to  $\lambda$ , whereas particles where  $\lambda$  does not exceed  $\sigma$  very much will be well described by the continuum theory only if the cluster size is smaller than yet comparable to  $\lambda$ . Hence, we refrain from cutting off the diagrams in Figure 9 at low pressures but we emphasize that such a cutoff exists and that it depends on the shoulder-to-core ratio.

## CONCLUSIONS

The continuum theory presented here predicts the same phenomenology of the core-corona colloids as the complementary methods including numerical simulations,<sup>17</sup> lattice theory,<sup>37</sup> and genetic-algorithm search of minimal-enthalpy structures.<sup>22–25</sup> Compared to the other approaches, its main advantages are the intuitive conceptual framework and a clear insight into the various terms in the thermodynamic potential. In addition, the model is relatively undemanding—the main challenge is to dissect the geometry of the overlap zones. As we have shown, this task can be somewhat simplified by noting that the shoulders of particles in a given cluster penetrate into but do not protrude through nearest-neighbor clusters and that the cluster size (i.e., the thickness or diameter) is smaller than the shoulder width.

In principle, the phase diagram could be extended to complex structures such as the more elaborate spherical and columnar lattices as well as the various bicontinuous phases.<sup>37</sup> The former present no special challenge, whereas the latter should be more tedious. However, we expect that the only bottleneck of the analysis is the description of the average overlap zone, and as we have shown in this study, the exact solution of the model should be more reliable than the approximate version. One could also consider mixed morphologies consisting, e.g., of coexisting spherical and cylindrical clusters, or of clusters of different sizes which could be relevant for the more exotic spherical phases such as the A15 lattice.<sup>11</sup> To the best of our knowledge, this possibility was not explored so far and the continuum model may well be the most straightforward way of testing it.

The analysis presented here can also be carried out for other types of shoulder pair potentials. We expect that for smooth shoulders, say the various algebraic potentials<sup>16,20</sup> or the so-called generalized exponential model,<sup>38</sup> the average overlap energy cannot be expressed in as simple a closed form as for square shoulders. However, the integrals involved can surely be evaluated numerically at a small fraction of cost and effort of, say, Monte Carlo or molecular-dynamics simulations. Thus, the approach may well be advantageous and preferred not only as a preliminary scan but also for a more in-depth study.

Another interesting generalization of the  $T = 0$  continuum theory of soft colloids is its finite-temperature version. The new ingredient needed is the entropy which disfavors the cluster phases where the particles occupy a part of the space rather than the whole volume like in the uniform phase. An important point to note is that a given particle is not confined to a specific cluster—instead, they hop from one cluster to another.<sup>39,40</sup> This suggests that the space that they are free to explore consists of the combined volume of all clusters, which is smaller than the total volume but still proportional to it. If we assume that each particle

experiences a more or less flat effective intracluster potential, the entropy of the ensemble can be approximated by that of a hard-core system at the effective density. Within the continuum model, this is best done by using the Carnahan-Starling formula for the liquid state and the cell theory for the crystalline state. The 2D version of the finite temperature model did recover the liquid and the solid variant of the disk and stripe clusters predicted by the Monte Carlo simulations<sup>21</sup> and could be applied to all 3D morphologies described above. However, at low enough temperatures, the stability of the cluster morphologies relative to the uniform phase relies much more on their respective energies which scale as  $\epsilon\lambda^3/\sigma^3$  (and depend on density) than on their entropies which are of the order of  $k_B T$ . This suggests that the main mechanism of clustering of hard-core/soft-shoulder particles is captured by the energetic considerations covered by the  $T = 0$  theory.

## AUTHOR INFORMATION

### Corresponding Author

\*E-mail: gernot.pauschenwein@ait.ac.at.

### Author Contributions

<sup>†</sup>These authors have contributed equally to the work.

## ACKNOWLEDGMENT

We thank M. A. Glaser for stimulating discussions. This work was supported by the Austrian Science Foundation under Project Nos. W004, P17823-N08, and P19890-N16, by the Slovenian Research Agency through Grant No. P1-0055, by the Marie-Curie Initial Training Network COMPLOIDS under FP7-PEOPLE-ITN-2008 Grant No. 234810, and by the bilateral Austrian-Slovenian Grant No. BI-AT/09-10-007.

## REFERENCES

- (1) Kincaid, J. M.; Stell, G.; Goldmark, E. *J. Chem. Phys.* **1976**, *65*, 2172–2179.
- (2) Young, D. A.; Alder, B. J. *Phys. Rev. Lett.* **1977**, *38*, 1213–1216.
- (3) Hemmer, P. C.; Stell, G. *Phys. Rev. Lett.* **1970**, *24*, 1284–1287.
- (4) Stell, G.; Hemmer, P. C. *J. Chem. Phys.* **1972**, *56*, 4274–4286.
- (5) Bolhuis, P.; Frenkel, D. *J. Phys.: Condens. Matter* **1997**, *9*, 381–387.
- (6) Lang, A.; Kahl, G.; Likos, C. N.; Löwen, H.; Watzlawek, M. *J. Phys.: Condens. Matter* **1999**, *11*, 10143–10161.
- (7) See, e.g.: Hemmer, P. C.; Velasco, E.; Mederos, L.; Navascués, G.; Stell, G. *J. Chem. Phys.* **2001**, *114*, 2268–2275.
- (8) McConnell, G. A.; Gast, A. P.; Huang, J. S.; Smith, S. D. *Phys. Rev. Lett.* **1993**, *71*, 2102–2105.
- (9) Hamley, I. W.; Daniel, C.; Mingvanish, W.; Mai, S. M.; Booth, C.; Messe, L.; Ryan, A. J. *Langmuir* **2000**, *16*, 2508–2514.
- (10) Lodge, T. P.; Bang, J.; Park, M. J.; Char, K. *Phys. Rev. Lett.* **2004**, *92*, 145501.
- (11) Zeng, X.; Ungar, G.; Liu, Y.; Percec, V.; Dulcey, A. E.; Hobbs, J. K. *Nature* **2004**, *428*, 157–160.
- (12) Lee, S.; Bluemle, M. J.; Bates, F. S. *Science* **2010**, *330*, 349–353.
- (13) Peterca, M.; Percec, V. *Science* **2010**, *330*, 333–334.
- (14) Hayashida, K.; Dotera, T.; Takano, A.; Matsushita, Y. *Phys. Rev. Lett.* **2007**, *98*, 195502.
- (15) Israelachvili, J. N. *Intermolecular and Surface Forces*; Academic Press: London, 1992.
- (16) Velasco, E.; Mederos, L.; Navascués, G.; Hemmer, P. C.; Stell, G. *Phys. Rev. Lett.* **2000**, *85*, 122–125.
- (17) Malescio, G.; Pellicane, G. *Nat. Mater.* **2003**, *2*, 97–100.
- (18) Camp, P. J. *Phys. Rev. E* **2003**, *68*, 061506.

- (19) Malescio, G.; Pellicane, G. *Phys. Rev. E* **2004**, *70*, 021202.
- (20) Jagla, E. A. *J. Chem. Phys.* **1999**, *110*, 451–456.
- (21) Glaser, M. A.; Grason, G. M.; Kamien, R. D.; Košmrlj, A.; Santangelo, C. D.; Zihlerl, P. *EPL* **2007**, *78*, 46004.
- (22) Fornleitner, J.; Kahl, G. *EPL* **2008**, *82*, 18001.
- (23) Fornleitner, J.; Kahl, G. *J. Phys.: Condens. Matter* **2010**, *22*, 104118.
- (24) Pauschenwein, G. J.; Kahl, G. *Soft Matter* **2008**, *4*, 1396–1399.
- (25) Pauschenwein, G. J.; Kahl, G. *J. Chem. Phys.* **2008**, *129*, 174107.
- (26) Likos, C. N.; Lang, A.; Watzlawek, M.; Löwen, H. *Phys. Rev. E* **2001**, *63*, 031206.
- (27) Imperio, A.; Reatto, L. *J. Phys.: Condens. Matter* **2004**, *16*, S3769–S3789.
- (28) Fornleitner, J. Ordered Equilibrium Structures of Two-Dimensional Soft Matter Systems. Ph.D. Thesis, Technische Universität Wien, Vienna, 2008; downloadable from <http://www.ub.tuwien.ac.at>.
- (29) For large  $\lambda/\sigma$ , the unit cell of the inverted phase includes a large number of particles. The current implementation of the genetic algorithm search of hard-core/square-shoulder MECs<sup>28,34</sup> can efficiently process crystal lattices with bases of no more than about 30 particles, which seems to be too few to describe the inverted morphologies either in 2D or in 3D. The one exception is the honeycomb lattice found for small  $\lambda/\sigma = 1.5^{22}$  which can be regarded as a single-particle-thick inverted disk phase. Thus, we conclude that the reasons for the absence of the inverted phases in the MEC phase sequences are technical rather than physical.
- (30) Matsen, M. W.; Schick, M. *Phys. Rev. Lett.* **1994**, *72*, 2660–2663.
- (31) Osterman, N.; Babić, D.; Poberaj, I.; Dobnikar, J.; Zihlerl, P. *Phys. Rev. Lett.* **2007**, *99*, 248301.
- (32) Pieranski, P. *Phys. Rev. Lett.* **1980**, *45*, 569–572.
- (33) Mladek, B. M.; Kahl, G.; Likos, C. N. *Phys. Rev. Lett.* **2008**, *100*, 028301.
- (34) Pauschenwein, G. J. Phase Behaviour of Colloidal Systems. Ph.D. thesis, Technische Universität Wien, Vienna, 2008; downloadable from <http://www.ub.tuwien.ac.at>.
- (35) Hamley, I. W. *Nanotechnology* **2003**, *14*, R39–R54.
- (36) Lamarche, F.; Leroy, C. *Comput. Phys. Commun.* **1990**, *59*, 359–369.
- (37) Shin, H.; Grason, G. M.; Santangelo, C. D. *Soft Matter* **2009**, *5*, 3629–3638.
- (38) Mladek, B. M.; Gottwald, D.; Kahl, G.; Neumann, M.; Likos, C. N. *Phys. Rev. Lett.* **2006**, *96*, 045701.
- (39) Moreno, A. J.; Likos, C. N. *Phys. Rev. Lett.* **2007**, *99*, 107801.
- (40) Coslovich, D.; Strauss, L.; Kahl, G. *Soft Matter* [Online early access]. DOI: 10.1039/C0SM00545B.